scientific reports

OPEN

C_{60} fullerene against SARS-CoV-2 coronavirus: an in silico insight

Vasyl V. Hurmach[1], Maksim O. Platonov[2], Svitlana V. Prylutska[1,3], Peter Scharff[4], Yuriy I. Prylutskyy[1] & Uwe Ritter[4]✉

Based on WHO reports the new SARS-CoV-2 coronavirus is currently widespread all over the world. So far > 162 million cases have been confirmed, including > 3 million deaths. Because of the pandemic still spreading across the globe the accomplishment of computational methods to find new potential mechanisms of virus inhibitions is necessary. According to the fact that C_{60} fullerene (a sphere-shaped molecule consisting of carbon) has shown inhibitory activity against various protein targets, here the analysis of the potential binding mechanism between SARS-CoV-2 proteins 3CLpro and RdRp with C_{60} fullerene was done; it has resulted in one and two possible binding mechanisms, respectively. In the case of 3CLpro, C_{60} fullerene interacts in the catalytic binding pocket. And for RdRp in the first model C_{60} fullerene blocks RNA synthesis pore and in the second one it prevents binding with Nsp8 co-factor (without this complex formation, RdRp can't perform its initial functions). Then the molecular dynamics simulation confirmed the stability of created complexes. The obtained results might be a basis for other computational studies of 3CLPro and RdRp potential inhibition ways as well as the potential usage of C_{60} fullerene in the fight against COVID-19 disease.

Viral infections are widespread; they make up 95% of all known human infectious diseases. The coronaviruses are single-stranded RNA viruses that infect vertebrates. With the emergence of SARS-CoV-2 (severe acute respiratory syndrome-coronavirus-2), there are now few coronaviruses that are known to infect humans. Before COVID-19, only SARS-CoV (serve acute respiratory syndrome-CoV) and MERS-CoV (middle east respiratory syndrome-CoV) caused disease[1–4]. Therefore, anticoronaviral drug discovery has been a small effort relative to that for other viral diseases such as influenza. Given the rapid spread of COVID-19 and its relatively high mortality, filling the gap for coronavirus-specific drugs is urgent.

The SARS-CoV-2 genome comprises 11 ORFs (open reading frames). At the 5′-terminus ORF1a/b encoded polyprotein 1a and 1b which could be split into 16 different proteins; e. g. PLpro (papain-like protease), 3CLpro (chymotrypsin-like protease)/Mpro (main proteinase), Nsp9 (non-structural protein 9) binding protein, RdRp (RNA-dependent RNA polymerase), RNA helicase, exo-ribonuclease, endo-ribonuclease[5–8]. Contrary, 3′-terminus encoded proteins like S-glycoprotein, nucleocapsid protein, and others[9]. So, according to the above, isn't surprising that the coronavirus life cycle comprises a number of potentially targetable steps, including endocytic entry into host cells (angiotensin-converting enzyme 2 (ACE2) and transmembrane protease serine 2 (TMPRSS2)), RNA replication, and transcription (helicase and RNA-dependent RNA polymerase (RdRp)), translation and proteolytic processing of viral proteins (3CLpro and PLpro), virion assembly, and release of new viruses through the exocytic systems[10].

Amidst the various viral proteins, few are irreplaceable for the virus life cycle. 3CLpro protein has a crucial role in the replication and expression of viral genes[11,12]. The active site of this protein contains a catalytic dyad, where His 41 acts as general acid–base and Cys 145 acts as a nucleophile. The RdRp in complex with essential co-factors Nsp7 and Nsp8 is essential for virus RNA replication[13,14]. Based on recent studies, RdRp needs to create a complex with Nsp7 and Nsp8, such association activates the possibility to replicate long RNA molecules[14,15]. Thus, 3CLpro and RdRp appear to be promising protein targets for the development of inhibitors to treat SARS-Cov-2[4,16–22].

The appearance of SARS-CoV-2 coronavirus with its real threat to human life requires the rapid development of innovative diagnostic tests and antiviral formulations. In this regards, nanobiomaterials represent alternative resource to fight coronaviruses at different stages of infection by selective action[23,24]. The main interest in carbon-based nanosystems lies precisely in their potential low toxicity[25,26] and specific virus inhibition mechanisms[27]. One of the promising candidates for carbon antiviral nanoformulation can be C_{60} fullerene[27,28]. The highly

[1]Taras Shevchenko National University of Kyiv, Kyiv 01601, Ukraine. [2]Institute of Molecular Biology and Genetics of NASU, Kyiv 03143, Ukraine. [3]National University of Life and Environmental Science of Ukraine, Kyiv 03041, Ukraine. [4]Institute of Chemistry and Biotechnology, Technical University of Ilmenau, 98693 Ilmenau, Germany. ✉email: uwe.ritter@tu-ilmenau.de

symmetric nanostructure, such as C_{60} fullerene, has extraordinary geometric affinity with icosahedral viruses[29]. The creation of nanobiomaterials on the same scale and with similar geometry is a fascinating possibility which can be used to foster interactions and build smart nanostructures for inhibition or inactivate virus replication. Although pristine C_{60} fullerene has very low solubility in water, it can form a stable colloidal solution[30], containing both single C_{60} molecules (0.72 nm) and their spherical-like aggregates, the size of which is comparable to the average particle size of SARS-CoV-2—about 120 nm in diameter[31]. The mechanism of C_{60} fullerene dispersal in aqueous solutions might be explained by a formation of a covalent bond between the hydroxyls and carbons in the C_{60} molecule cage, as a result of ultrasound treatment that culminates in a consequent easy C_{60} fullerene dissolution[32]. Due to hydrophobicity, C_{60} fullerene easily penetrates the biological membrane by passive diffusion or endocytosis[33,34]. C_{60} fullerene serves as an enzyme inhibitor, drug delivery vector, contrast agent for MRT and photodynamic therapy[33,35–37]. Due to the presence of double electron-deficient chemical bonds in the structure, C_{60} fullerene easily attaches free radicals, i.e. is a powerful antioxidant[38–40], able to effectively exhibit the anti-inflammatory, antibacterial, antitumor, neuro- and radioprotective effects in the in vitro and in vivo systems[35,36,41,42]. Finally, importantly, C_{60} fullerenes and their water-soluble derivatives exhibit remarkable antiviral activity[27,28,35,36].

Thus, in this work we first analyzed available 3CLpro and RdRp structures and their possibility to interact with C_{60} fullerene employing computational methods. For this purpose, C_{60} fullerene was docked into 3CLpro and RdRp according to obtained binding models (in the case of 3CLpro, it is blocking of a catalytic dyad, for RdRp—blocking of RNA synthesis pore and preventing of binding with Nsp8). Then the molecular dynamics (MD) simulation was performed on obtained "C_{60} fullerene-3CLpro or RdRp" complexes. Subsequently, received MD trajectories were a subject of MMPBSA (molecular mechanics Poisson–Boltzmann surface area) as well as MMGBSA (molecular mechanics-generalized Born surface area) free-energy analysis. We believe that our computational results shed light on possible ways of 3CLpro and RdRp inhibition by nanobiomaterials, reveal the main flexibility properties of investigated targets and indicate favorable and unfavorable amino acid for interaction in selected binding pockets.

Calculation methods

Construction of "C_{60} fullerene-3CLpro or RdRp" systems. According to available structure data[43,44], the X-ray structures of monomeric 3CLpro protein (Protein Data Bank (PDB) ID 6M2N)[45] and RdRp protein (PDB ID 7BV2)[44] were retrieved from the RCSB PDB[42]. Firstly, all routine water molecules and native ligands were removed from the protein structure. Then prior to identifying binding pockets the protein structure treatment was done by the addition of missing hydrogen, correcting protonation states of amides, repairing side chains, and in the end, energy minimized. To run molecular docking simulation, the possible binding pockets for C_{60} fullerene were defined by Caver software cavity computational algorithm[46] and based on literature analysis[14,21,45,47–50]. As a result, three and one possible binding pockets were identified for RdRp and 3CLpro, respectively.

To each target molecular docking was carried out utilizing flexible C_{60} fullerene molecule and rigid 3CLpro or RdRp molecule. The systematic docking algorithm was used (SDOCK+)[51], implemented in the QXP package[52] (the method demonstrates all possible conformations of the studied structures with a minimum RMSD (root-mean-square deviation) value[51]). The maximum number of SDOCK routine steps was set to 300, and the 10 best complexes based on the built-in QXP scoring function[52] were selected for analysis in the next stages of the investigation. The optimal structure of the studied "C_{60} fullerene—3CLpro or RdRp" complexes was determined by the following basic criteria: (1) the area of the contact surfaces of the protein and ligand; (2) the distance between the 3CLpro or RdRp and C_{60} fullerene; (3) the energy characteristics of the binding in the formed complex. As a result of molecular docking to each study one (best) "C_{60} fullerene-3CLpro or RdRp" complex was selected.

MD simulation protocol. To estimate stability and crucial interactions of obtained complexes after molecular docking, MD simulation was performed. The calculations were done using Gromacs[53] 5.1.3 in force field[54] Charmm36. All exploring 3CLpro or RdRp were protonated according to the build-in function in Gromacs 5.1.3. The topology for C_{60} fullerene was generated by SwissParam[55]. The complexes obtained after molecular docking were used for MD simulation. Each system was placed into the center of a periodic cubic box which was then filled with TIP3P water molecules. A minimum 0.9 nm distance was maintained between the nearest atom of the complex and the edge of the simulation box so that the complex can fully immerse with water and rotate freely. Then, to neutralize the system and mimic the cellular environment (pH = 7), Na^+ and Cl^- ions were added to bring the ionic concentration to 150 mM. Here, the solvent molecules are replaced with monoatomic ions, randomly. Next, the obtained complex was energy minimized what also relieved any steric clashes. The system was relaxed by applying the steepest descent algorithm (the maximum number of steps was 50,000). Then the equilibration was computed in two stages: NVT was first equalized at 100 ps, with the second NPT equalization of 1 ns. After that, we launched MD simulation within 50 ns.

Note, that MD simulation was performed 3 times to each investigated "C_{60} fullerene—3CLpro or RdRp" complex. All calculations were done at the temperature of 300 K and at constant atmospheric pressure.

Binding free energy calculations. The binding energies of each complex were calculated by applying the MMPBSA method of g_mmpbsa toll[56] according to the following equation[57,58]

$$G_{binding} = G_{complex} - \left(G_{protein} + G_{ligand}\right),$$

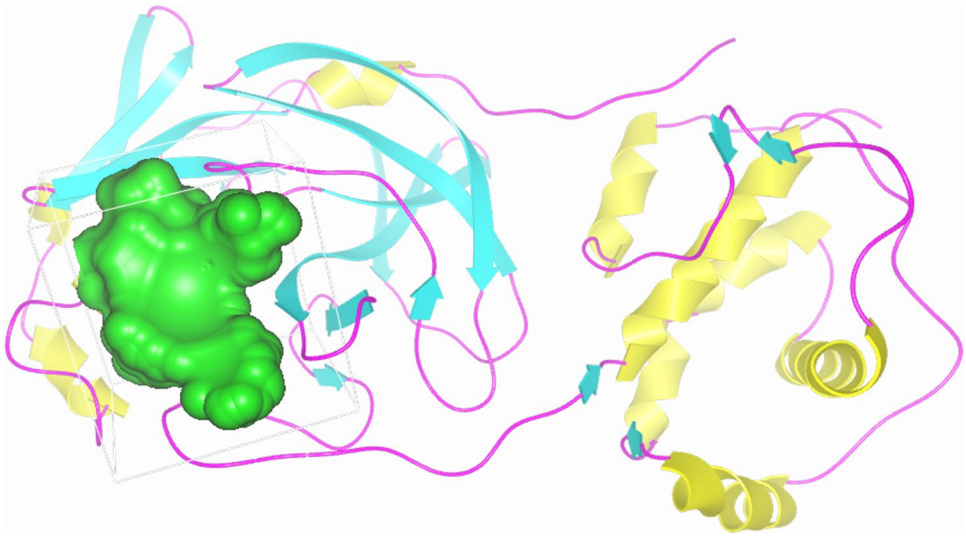

Figure 1. 3CLpro secondary structures and potential binding pocket for C_{60} fullerene (blue).

where $G_{complex}$: total free energy of "C_{60} fullerene-3CLpro or RdRp" complex, $G_{protein/ligand}$: total free energies of the isolated protein and ligand in a solvent, respectively. And then each parameter was estimated as follows

$$G_x = G_{mm} - T\Delta S + G_{solvatation},$$
$$G_{mm} = E_{bonded} + E_{nonbonded},$$
$$G_{solvatation} = G_{polar} + G_{nonpolar},$$

where x—"C_{60} fullerene-3CLpro or RdRp" complex or just separate protein or C_{60} fullerene, G_{mm}—average molecular mechanics potential energy in a vacuum (comprise energy of bonded (E_{bonded}) and nonbonded ($E_{nonbonded} = E_{vdW} + E_{elect}$, where E_{vdW}—van der Waals energy and E_{elect}—electrostatic energy) interactions and calculated based on the molecular mechanics force-field parameters)[59–61], TΔS—entropic contribution to the system, $G_{solvatation}$—the solvatation free energy (energy required to transfer a solute from vacuum into the solvent).

So, here the Poisson–Boltzmann (PB) equation has solved to estimate polar desolvation energy (G_{polar})[62]. In the PB calculations the grid size was 0.5 Å. The solvent dielectric constant and solute dielectric constant value was 80 and 2, respectively. Nonpolar ($G_{nonpolar}$) contribution was obtained based on solvent accessible surface area (SASA, $Å^2$)

$$G_{nonpolar} = \gamma SASA + b,$$

where γ—surface tension of the solvent and b—fitting parameter[63].

Next MMGBSA technique was used to obtain more precise picture of "C_{60} fullerene-3CLpro or RdRp" interaction[64,65]. The essential idea of MMGBSA is the estimation of binding energy between each residue of 3CLpro or RdRp and C_{60} fullerene. The algorithm of the MMGBSA method is the same as in MMPBSA and presented above. The whole energy parameters were calculated by utilizing all snapshots from the MD simulation trajectory of length 50 ns.

Result and discussion

Binding pocket determination. According to the surface analysis of 6M2N and available literature data[21,22,66–68], the only binding pocket capable of interacting with C_{60} fullerene was identified (Fig. 1).

It is a catalytic binding pocket. This pocket occupies volume 892 $Å^3$ and contains amino acids (Met 165, Met 49, Tyr 54, Cys 44, His 41, and Cys 145), which are able to create stacking interactions with C_{60} fullerene. Furthermore, taking into account that this binding pocket directly mediate the mutation of different Nsp[21,69,70], which are crucial for the virus life cycle, it make 3CLpro a perspective target for drug development against SARS-CoV-2[17,21,22].

As a result of surface and literature investigation of RdRp, three binding pockets were found. It is well known that RdRp plays a key role in SARS-CoV-2 RNA synthesis[14]. Based on our result two binding models between C_{60} fullerene and RdRp were indicated: model 1–C_{60} fullerene binding in RNA synthesis channel and model 2—simultaneous binding of C_{60} fullerene with pocket 2 and 3 (Fig. 2). So, by blocking the RNA synthesis channel the RNA synthesis procedure will be impossible[19,21,71]. That is why the first detected binding pocket locates in the RNA synthesis channel (Fig. 2). On the other hand, without the assistance of Nsp7 and Nsp8 as co-factors RdRp is not able to carry out its initial functions[14,72,73]. Based on these two other pockets were found in the RdRp-Nsp8 binding interface (Fig. 2). All found binding pockets comprise at least two amino acids, which can create any stacking interactions with C_{60} fullerene. For example, pocket 1 contains Arg 570, Lys 578 and Tyr 690.

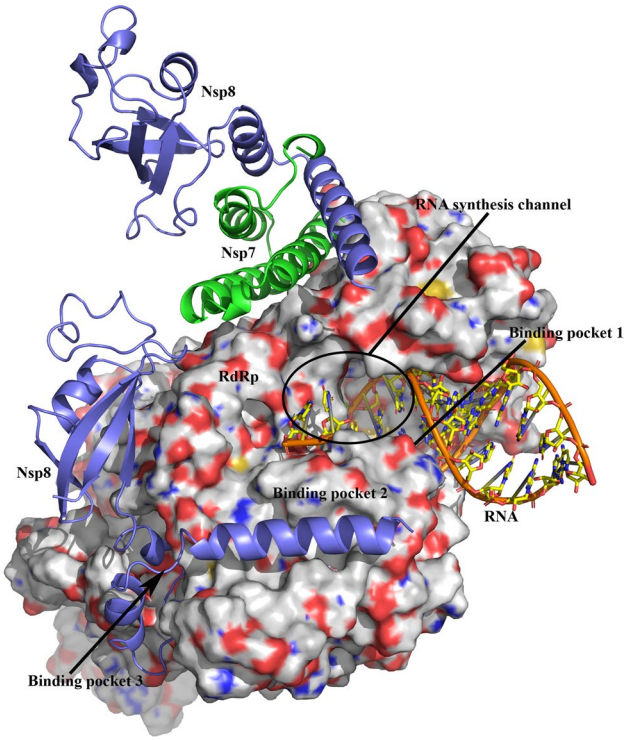

Figure 2. Structure of SARS-CoV 2 RdRp (surface presentation) in complex with Nsp7 (in green), Nsp8 (in purple) co-factors and RNA molecule (stick model). In one case RdRp directly interacts with Nsp8, in other it binds to heterodimer of Nsp7 and Nsp8. Pocket 1 locates in RNA synthesis channel, pockets 2 and 3 locate in direct binding interface between RdRp and Nsp8.

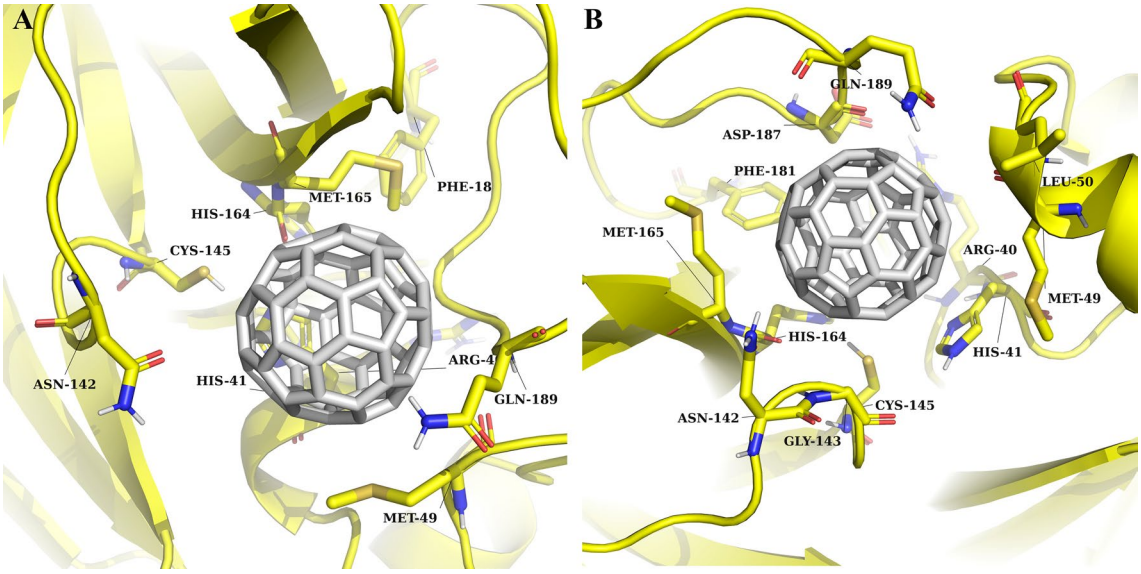

Figure 3. Catalytic binding pocket of 3CLpro: 3CLpro highlighted in yellow, and C_{60} fullerene in grey. Molecular docking result (**A**); MD simulation result (**B**).

Molecular docking. *3CLpro* in the presented binding model, C_{60} fullerene is tightly stuck in the catalytic binding pocket. It results in catalytic dyad shielding from interacting with any other molecular structures. There, C_{60} fullerene lies above catalytic His 41 and creates direct stacking interaction with one. Moreover, in this part of 3CLpro catalytic binding pocket C_{60} fullerene creates stacking interaction with Cys 145, Met 49, Met 165, Met 49 and steric interactions with Gln 189 and Asn 142 (Fig. 3A). More importantly, those amino acids are located on different sides of the catalytic binding pocket, and as an outcome, they clamp C_{60} fullerene in the catalytic binding pocket.

RdRp as with 3CLpro, C_{60} fullerene filled in selected binding pockets of RdRp and tightly clamped there by different stacking and steric interactions (Fig. 4A,C,E). The inhibition of pocket 1 could cause blocking of RNA synthesis channel (Figs. 2, 4A). Here, C_{60} fullerene fits perfectly to the binding pocket and makes π-cation interactions with Arg 570 and Lys 578, T-stacking with Tyr 690, and steric interactions with Asn 497 and Leu 577. Conversely, the C_{60} fullerene interaction with pocket 2 or 3 depicts the model which prevents complex formation between RdRp and Nsp8 (Figs. 2, 4C,E). As a result, RdRp is not able to carry out its initial functions. So, in pocket 2 the bottom part of C_{60} fullerene stacks between Trp 510, Phe 369 and Leu 372, Leu 515 by stacking and steric interactions, respectively. Additionally, Tyr 516 and Phe 507 are located at the bottom of the binding pocket (Fig. 4C). These two amino acids possibly are capable of holding C_{60} fullerene in the current position by stacking interaction. In spite of mentioned above the stability of the obtained complex is questionable because the binding pocket itself isn't deep. Because of such a flat surface geometry of pocket 2, C_{60} fullerene could be forced out of this binding pocket. Despite the fact that in pocket 3 almost not presents any aromatic amino acid which is able to create stacking interactions with C_{60} fullerene, we think that pocket 3 is promising because of its depth. Here, C_{60} fullerene creates steric interactions with Ala 384, Val 331, Val 399, Thr 325, and Leu 271. Also, the binding pocket contains Phe 397 and Tyr 274, which are spatially close to docked C_{60} fullerene. So, there is a possibility of stacking interaction with those amino acids.

The molecular docking results suggested that in all selected binding pockets C_{60} fullerene is able to create a stable complex with 3Clpro and RdRp targets. The binding with 3CLpro is characterized by one possible binding model. For the RdRp, model 1 (interaction in pocket 1) and model 2 (simultaneous interaction with pockets 2 and 3) were investigated.

MD analysis. To obtain more accurate results, 50 ns MD simulations were carried out (Figs. 3, 4, 5, 6). The MD results showed that each investigated "C_{60} fullerene-3CLpro or RdRp" are stable. The RMSD movement during MD simulation of each complex is in a range 2–3 Å (Fig. 5). Furthermore, in some examples C_{60} fullerene is able to form new and more profitable interactions.

3CLpro the simulated complex is shown in Fig. 3B. For 3CLpro, it was observed that C_{60} fullerene shifts by 3.2 Å and caused Asn 142 displacement for 4.8 Å toward C_{60} fullerene. In contrast, C_{60} fullerene forced out Gln 189 for 1.8 Å from the catalytic binding pocket. The binding with amino acids like Met 156, Phe 181, His 164, and others are without any fundamental changes. The more intriguing is that both His 41 and Cys 145 (catalytic dyad) are forced out from their initial position by C_{60} fullerene, either. As a result, the integrity of the catalytic dyad is violated and without any doubt, it has a negative impact on 3CLpro functionality. The "C_{60} fullerene-3CLpro" complex was then subjected to RMSF (root-mean-squared-fluctuation) investigation. No, any extreme fluctuations compare to the free form of the 3CLpro molecule were detected (Fig. 6A). For example, the flexibility of His 41 in free and bond to C_{60} fullerene form are 0.8 and 1.4 Å, respectively. Moreover, in the case of the "C_{60} fullerene-3CLpro" complex, the reduction of fluctuation values was determined.

RdRp according to the MD simulation result in a case of pockets 1 and 2 the fluctuations of C_{60} fullerene inside both binding pockets (4.1 Å and 3.5 Å, respectively) without significant changes in obtained complexes (Fig. 4B,D) were observed. And, in pocket 3 opposite picture was detected. Here, C_{60} fullerene immersed inside the binding pocket by 4.0 Å. Anyway, the key interactions between C_{60} fullerene and RdRp in whole models remain (Fig. 4B,D,F). So, almost no changes were indicated during MD simulation for pocket 1. Here, it is possible to say that amino acids Ile 590, Tyr 690, Leu 577, and Gln 574 are rigid and just slightly change their initial position during MD simulation (< 0.75 Å), those amino acids interact with C_{60} fullerene by strong steric interactions. Contrarily, Lys 578 and Arg 570 are more flexible and characterized by some displacement (1.5 Å and 1.6 Å, respectively). Interestingly, that the π-cation interaction with Lys 578 isn't stable, but with Arg 570 is stable. Arg 570 is tightly locked to C_{60} fullerene. Such difference in the interactions between C_{60} fullerene and Lys 578/Arg 570 could be related with the location of those amino acids in the binding pocket. The Lys 578 locates on the edge of the pocket and can freely move (especially, because of Lys amino acid long linker) in contrast Arg 570 locates inside the binding pocket and has less space for movement. In pocket 2 (Fig. 4E) C_{60} fullerene stuck in the insight the pocket, creating steric interaction with Leu 372, Leu 515, and stacking with Phe 369 and Trp 510. Notably, during the whole MD simulation trajectory, the displacement of key binding amino acids (e.g. Phe 369, Trp 510, Tyr 516, Leu 315 and Leu 367) is minimal, about 1 Å. Also, we think that in this position C_{60} fullerene is held by stacking interaction with Tyr 516, which locates in the bottom of the binding pocket 2. Thus, the distance between C_{60} fullerene and Tyr 516 is about 3 Å during all MD simulation. Finally, in pocket 3 inverted picture compare to the above has observed (Fig. 4F). C_{60} fullerene shifted inside the binding pocket and tightly stacked among the surrounding hydrophobic amino acids by interacting with RdRp via stacking and steric interactions with Phe 397 and Val 399, Ala 384, Val 331, Thr 325, respectively. Those interactions become possible due to the shift of Phe 397 (4.9 Å), Val 399 (3.5 Å), and Ala 384 (3.2 Å). Other amino acids Val 331 and Thr 235 located in pocket 3 almost not shifted (about 0.5 Å). As for the previous target, here RMSF analysis has been done as well (Fig. 6B). So, the amino acids 324–342 and 364–410 in the case of C_{60} fullerene binding in pockets 2 and 3 are more flexible compare to the model, where C_{60} fullerene bond to pocket 1 and to unbound RdRp. It is not surprising and could be simply explained by shifting and immersion of C_{60} fullerene in the binding pockets 2 and 3. Of course, during the shifting/immersion C_{60} fullerene in some level pushes amino acids, and it resulted in their mobility. However, in a model with C_{60} fullerene bond pocket 1 mirrored situation is observed. Here, the flexibility of amino acids 840–862 is greater compare to their flexibility in the case of unbound RdRp or bond to pocket 2 and 3. Such a result was obtained due to the fact that in the case of C_{60} fullerene binding in pocket 1 RNA molecule isn't present in RNA synthesis pore (there isn't enough space for RNA molecule).

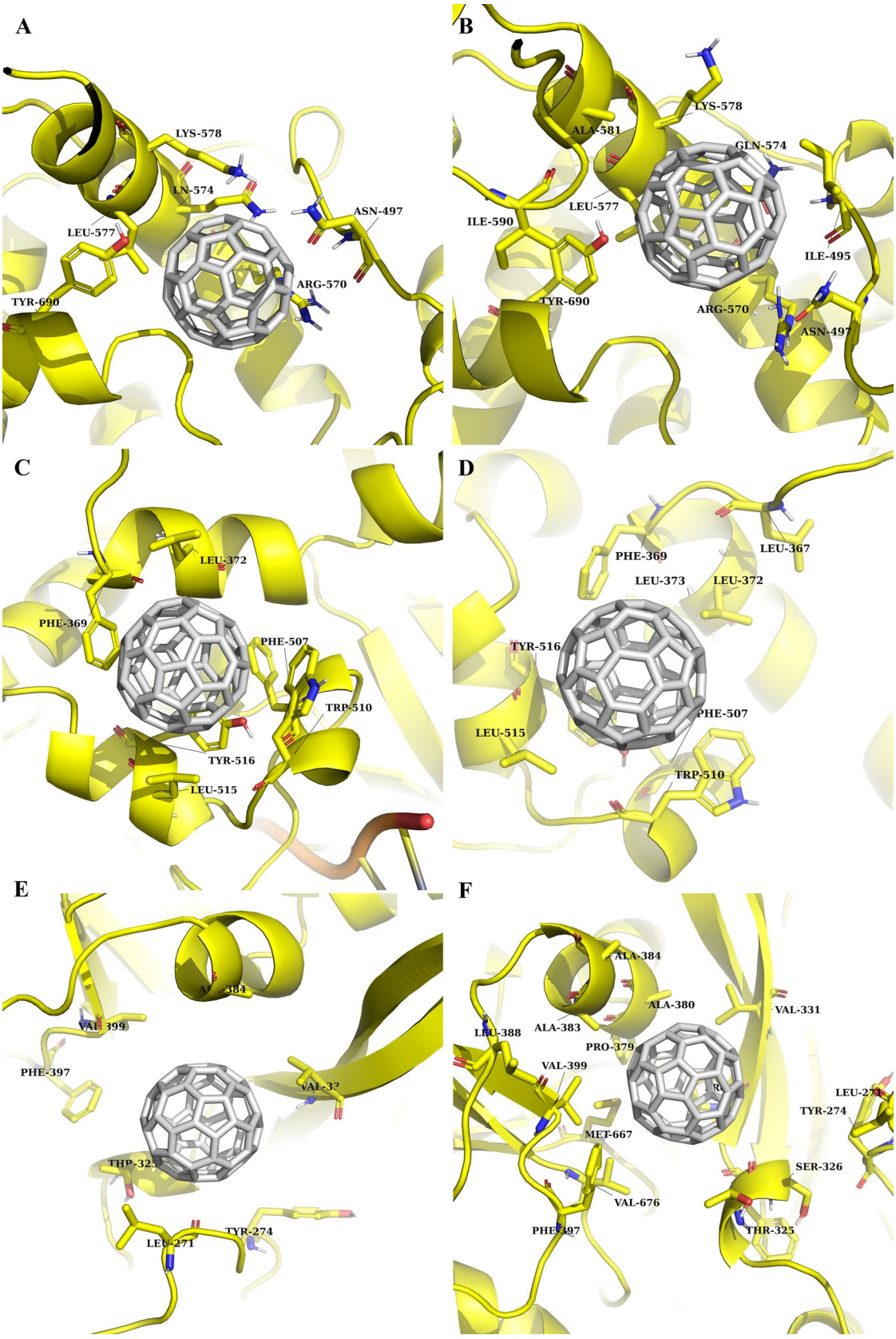

Figure 4. Molecular docking (**A**, **C**, **E**) and MD simulation (**B**, **D**, **F**) results of complex between C_{60} fullerene (in grey) and investigated pockets of RdRp (in yellow): (**A**, **B**)—pocket 1; (**C**, **D**)—pocket 2; (**E**, **F**)—pocket 3.

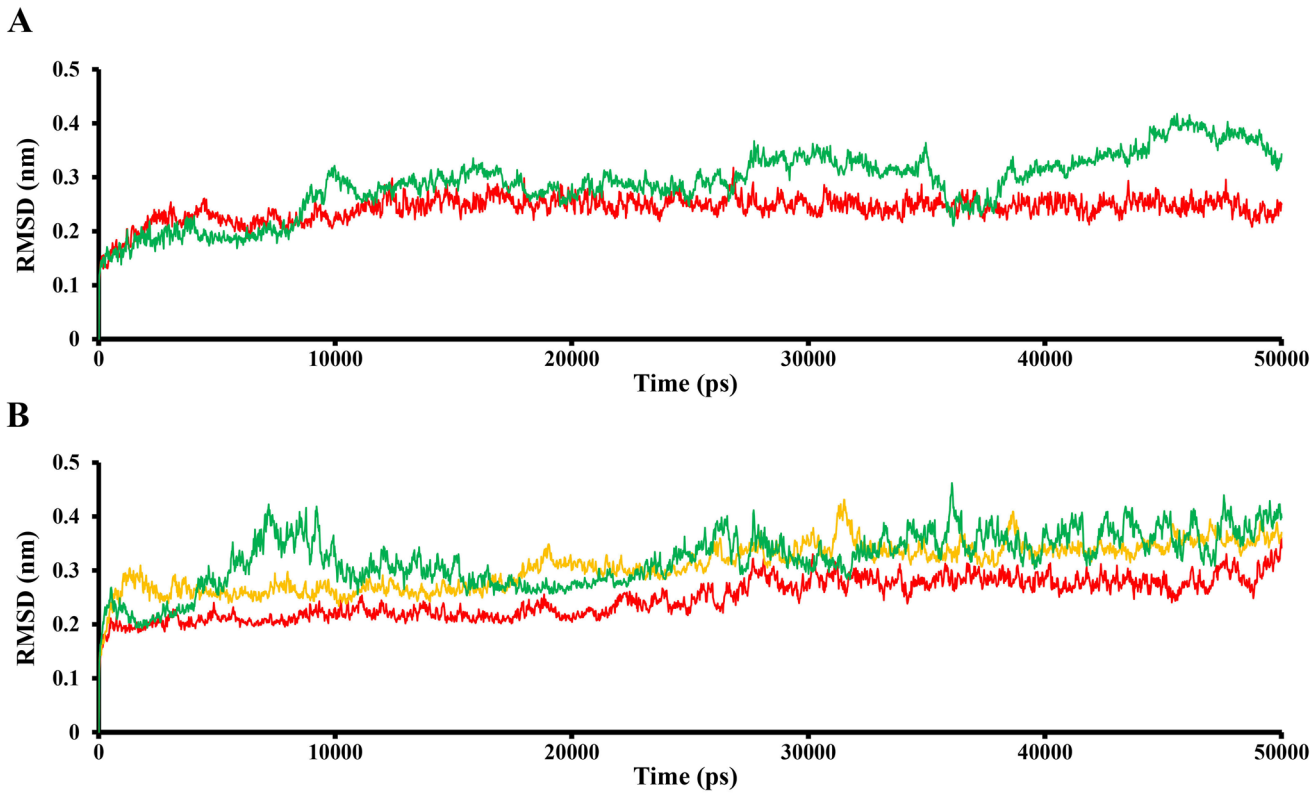

Figure 5. RMSD trajectories of 3CLpro (**A**) and RdRp (**B**) complexes with C_{60} fullerene: 3CLpro free protein molecule—green, "C_{60} fullerene-3CLpro" complex—red, and RdRp free protein molecule—green, "C_{60} fullerene-RdRp" pocket 1 (binding model 1)—red, "C_{60} fullerene-RdRp" pocket 2/3 (binding model 2)—orange.

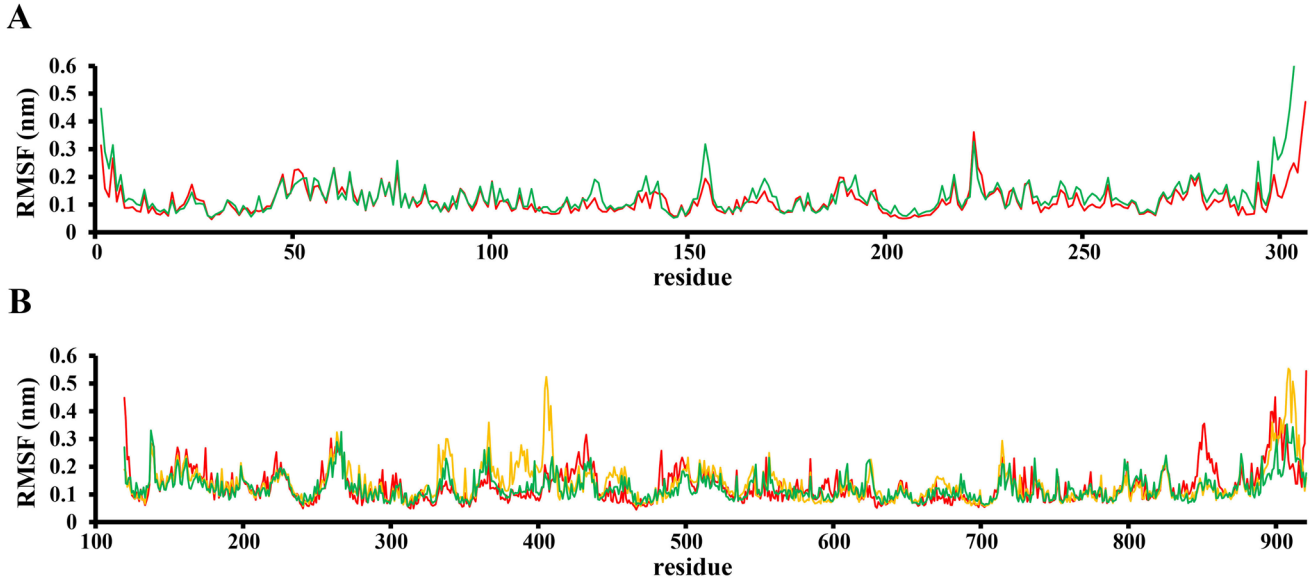

Figure 6. RMSF of the 3CLpro (**A**) and RdRp (**B**) in complex with C_{60} fullerene: 3CLpro free protein molecule—green, "C_{60} fullerene-3CLpro" complex—red, and RdRp free protein molecule—green, "C_{60} fullerene-RdRp" pocket 1 (binding model 1)—red, "C_{60} fullerene-RdRp" pocket 2/3 (binding model 2)—orange.

MMPBSA approach. The potential binding affinities within "C_{60} fullerene-3CLpro or RdRp" complexes were estimated by the MMPBSA analysis. Table 1 suggests that the $G_{binding}$ in "C_{60} fullerene-3CLpro or RdRp pocket 3" complexes are more favorable compare to "C_{60} fullerene-RdRp pocket 1/2". Next, for a better understanding of which energy type has a bigger contribution to complex formation and stability, each separate energy component was analyzed. From Table 1 it can be found that E_{vdW} has the largest contribution to the binding energy of the C_{60} fullerene with 3CLpro and RdRp. As previously, the E_{vdW} values of "C_{60} fullerene-3CLpro or

Contribution (kJ/mol)	3CLPro	RdRp		
		Pocket 1	Pocket 2	Pocket 3
E_{vdW}	− 204.275 ± 18.0	− 164.9 ± 16.7	− 126.3 ± 20.9	− 178.9 ± 13.4
E_{elect}	− 0.016 ± 1.4	0.08 ± 2.3	− 0.185 ± 1.15	0.007 ± 1.951
G_{polar}	60.8 ± 9.4	46.1 ± 9.5	21.1 ± 12.8	34.1 ± 4.4
$G_{nonpolar}$	− 15.8 ± 1.4	− 12.8 ± 1.2	− 9.9 ± 1.5	− 13.8 ± 1.2
$G_{binding}$	− 159.3 ± 15.2	− 131.5 ± 15.3	− 115.4 ± 23.8	− 158.5 ± 12.5

Table. 1. The energetic parameters obtained from MMPBSA investigation.

RdRp pocket 3" complexes are far better compare to "C_{60} fullerene-RdRp pocket 1/2". The other calculated energies (E_{elect}, G_{polar} and $G_{nonpolar}$) are positive or close to null. That is why their impact on complex formation and especially stability is unfavorable. However, the E_{elect} and $G_{nonpolar}$ contributions are lightly favorably than G_{polar}. Anyway, this slightly bigger effect of E_{elect} and $G_{nonpolar}$ is not much more noticeable in comparison with G_{polar}.

MMGBSA approach. To get a more precise binding energy characterization of obtained complexes, a per-residue free-energy decomposition study was performed. According to the results presented in Fig. 7 the most favorable contribution in all models is done by amino acids, which are able to create stacking interaction with C_{60} fullerene. However, some exceptions are detected (e.g. "C_{60} fullerene-RdRp pocket 1").

3CLpro Fig. 7 A emphasizes the role of the catalytic dyad in the binding process. The His 41 and Cys 145 have a positive effect on binding with C_{60} fullerene and the binding energy is -4.63 and -3.88 kJ/mol, respectively. As was mentioned above, due to this, the C_{60} fullerene can immerse into the 3CLpro catalytic binding pocket. Nevertheless, the binding contribution of the catalytic dyad isn't most favorable. The amino acids Met 49 (binding energy with C_{60} fullerene is − 5.54 kJ/mol), Met 165 (− 8.18 kJ/mol), Leu 50 (-3.99 kJ/mol), Gly 143 (− 2.58 kJ/mol), Asp 187 (− 2.83 kJ/mol) and Gln 189 (− 5.25 kJ/mol) clamp C_{60} fullerene in the binding pocket by stacking and steric interactions (Figs. 3B, 7A). Surprisingly, contrary to the above Arg 40 (6.94 kJ/mol) causes the destabilization of the "C_{60} fullerene–3CLpro" complex formation. This can be explained by the fact C_{60} fullerene prevents the interaction of Arg 40 with water molecules which usually in abundance in any binding pocket.

RdRp the comparison of key amino acids in pocket 1 has shown that steric interactions with C_{60} fullerene here are the most favorable (Fig. 7B). Among the whole residue, the interaction between C_{60} fullerene and Ile 49 (− 5.78 kJ/mol), Asn 497 (− 2.67 kJ/mol), Leu 557 (− 6.89 kJ/mol), Lys 578 (− 5.71 kJ/mol), Ala 581 (− 4.68 kJ/mol), Ile 590 (− 2.65 kJ/mol) and Gly 591 (− 2.89 kJ/mol) are far better compared to other amino acids in binding pocket 1. And what is interesting, only one of them forms π-cation interaction (Lys 578) with C_{60} fullerene. Because C_{60} fullerene is an aromatic system and preferably creates different stacking interactions it can cause a negative effect on complex stability. As previously, few amino acids destabilize C_{60} fullerene in binding pocket 1, namely: Arg 570 (2.31 kJ/mol) and Tyr 690 (1.25 kJ/mol). For the binding in pocket 2 stacking interactions are favorable (Figs. 4D, 7C). As follows from the Fig. 7C such amino acids as Leu 367 (− 2.16 kJ/mol), Phe 369 (− 8.64 kJ/mol), Leu 372 (− 5.58 kJ/mol), Leu 373 (- kJ/mol), Phe 507 (− 1.51 kJ/mol), Tpr 510 (− 9.76 kJ/mol), Leu 515 (− 6.04 kJ/mol) and Tyr 516 (− 4.42 kJ/mol) create strong interaction with C_{60} fullerene. Contrary to other investigated binding pockets in this case no amino acid has a huge unfavorable impact on "C_{60} fullerene–RdRp pocket 2" complex formation. From Fig. 7D it can be seen that the interactions between C_{60} fullerene and RdRp pocket 3 are mainly determined by the following residues Ser 326 (− 1.53 kJ/mol), Thr 325 (− 1.95 kJ/mol), Pro 329 (− 2.14 kJ/mol), Val 331 (− 5.42 kJ/mol), Pro 379 (− 3.64 kJ/mol), Ala 380 (− 4.98 kJ/mol), Ala 383 (− 3.48 kJ/mol), Leu 388 (− 1.88 kJ/mol), Phe 397 (− 5.73 kJ/mol), Val 399 (− 5.04 kJ/mol), Met 667 (− 4.86 kJ/mol) and Val 676 (− 3.86 kJ/mol). Here, we can observe the mix of favorable steric and stacking interactions between C_{60} fullerene and pocket 3. For example, the most strongly C_{60} fullerene interacts with Vall 331, Ala 380, Val 339, and Val 676 by steric interactions and despite above by stacking interaction with Pro 379, Phe 397, and Met 667. And finally in this case the C_{60} fullerene interaction with Phe 327 is unfavorable. That can be related to the fact that only the peptide backbone of Phe 327 interacts with C_{60} fullerene. Furthermore, this part of the backbone by C_{60} fullerene isolated from a solvent, what possible is able to cause such tension between those molecular parts/structures.

Summarizing, the in silico approach allows simulating the behavior of C_{60} fullerene in the binding sites of SARS-CoV-2 coronavirus and thus to predict the therapeutic effect of this unique molecule. A complementary interaction of C_{60} fullerene with proteins is a basis of its biomedical effects[74–77]. So, molecular docking and MD simulation were carried out using Toll-like receptors (TLRs play extremely critical roles in maintaining the immune-homeostasis of the human body) including TLR4[75]. The binding of C_{60} fullerene with TLR4 is characterized by complete filling of the hydrophobic pocket of MD-2 domain and the formation of a significant number of stacking interactions (e.g. with Phe 119, Phe 76 and Phe 104). This change of binding site is associated with significant mobility of interacting components: RMSD value for protein is 4.6 Å, and for C_{60} fullerene—5.3 Å. The obtained "C_{60} fullerene-TLR4" complex was characterized by a high energy: − 50 kJ/mol. In a recent study[78], spike protein of SARS-CoV-2 was found to interact with the extracellular domain of the cell surface TLRs. Intriguingly, the highest binding affinity and strength were evident in the "spike protein-TLR4" complex. Thus, the usage of C_{60} fullerene to inhibit TLR4 as well as 3CLpro and RdRp activation may be an effective strategy to treat COVID-19.

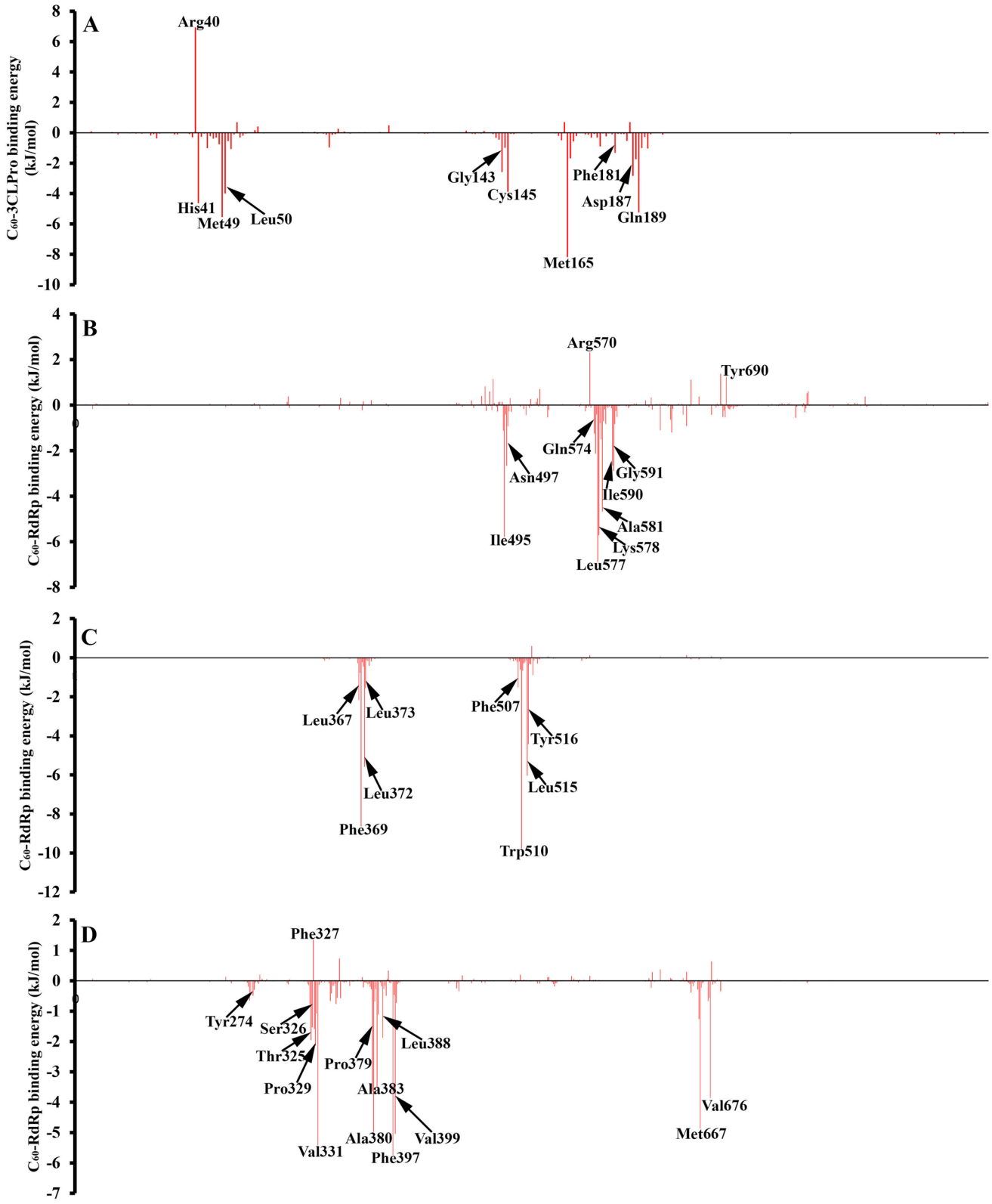

Figure 7. Per-residue binding energy decomposition of investigated complexes: "C_{60} fullerene-3CLpro" (**A**); "C_{60} fullerene-RdRp" pocket 1 (**B**); "C_{60} fullerene-RdRp" pocket 2 (**C**); "C_{60} fullerene-RdRp" pocket 3 (**D**).

Conclusion

The computer simulations (docking and molecular dynamics) we presented here suggest that C_{60} fullerene is able to block 3CLpro (blocking of catalytic dyad) and RdRp (blocking model 1 and 2) protein targets of SARS-CoV-2 coronavirus with different mechanisms and suppress its functional activity. The simulations revealed that in all investigated complexes C_{60} fullerene filled in the binding pocket and stuck there by the stacking and steric interactions. Critically that for 3CLpro C_{60} fullerene violated catalytic dyad integrity. All the other changes during simulations there weren't significant. In the case of RdRp pockets 1 and 2, C_{60} fullerene just fluctuates inside the binding pockets without fundamental changes of previously obtained complexes. The reverse picture has been observed in RdRp pocket 3, here C_{60} fullerene immerses inside the binding pocket and stuck there. The MMPBSA study has shown that in all cases $G_{binding}$ is more favorable in the case of "C_{60} fullerene-3CLpro or RdRp pocket 3" complexes compare to others. And as the main component, E_{vdW} has the biggest contribution to all complexes. Furthermore, the contribution of E_{elect}, G_{polar}, and $G_{nonpolar}$ are questionable and most of all are unfavorable because of that energies proximity to null or in some cases that energies are far bigger than null. And finally based on MMGBSA investigation favorable and unfavorable amino acids for complex formation with C_{60} fullerene were detected. The results of the study can provide understanding of 3CLpro and RdRp binding with other nanobiomaterials. Moreover, since the pristine C_{60} fullerenes can form a high stable aqueous colloidal solution and exhibit anticoronavirus activity, this expands their use for prophylactic and therapeutic purposes, which requires further in vitro and in vivo testing.

Received: 9 March 2021; Accepted: 24 August 2021
Published online: 07 September 2021

References

1. Lipsitch, M. *et al.* Transmission dynamics and control of severe acute respiratory syndrome. *Science* **300**(5627), 1966–1970. https://doi.org/10.1126/science.1086616 (2003).
2. Sharif-Yakan, A. & Kanj, S. S. Emergence of MERS-CoV in the Middle East: origins, transmission, treatment, and perspectives. *PLoS Pathog* **10**(12), e1004457. https://doi.org/10.1371/journal.ppat.1004457 (2014).
3. Song, Z. *et al.* From SARS to MERS, thrusting coronaviruses into the spotlight. *Viruses* **11**(1), 59. https://doi.org/10.3390/v11010059 (2019).
4. Muteeb, G., Alshoaibi, A., Aatif, M., Rehman, M. T. & Qayyum, M. Z. Screening marine algae metabolites as high-affinity inhibitors of SARS-CoV-2 main protease (3CLpro): an in silico analysis to identify novel drug candidates to combat COVID-19 pandemic. *Appl. Biol. Chem.* **63**(1), 79. https://doi.org/10.1186/s13765-020-00564-4 (2020).
5. Snijder, E. J., Decroly, E. & Ziebuhr, J. The nonstructural proteins directing coronavirus RNA synthesis and processing. *Adv. Virus Res.* **96**, 59–126. https://doi.org/10.1016/bs.aivir.2016.08.008 (2016).
6. Zumla, A., Chan, J. F., Azhar, E. I., Hui, D. S. & Yuen, K. Y. Coronaviruses—drug discovery and therapeutic options. *Nat. Rev. Drug. Discov.* **15**(5), 327–347. https://doi.org/10.1038/nrd.2015.37 (2016).
7. Ruan, Z. *et al.* SARS-CoV-2 and SARS-CoV: Virtual screening of potential inhibitors targeting RNA-dependent RNA polymerase activity (NSP12). *J. Med. Virol.* https://doi.org/10.1002/jmv.26222 (2020).
8. Chen, Y., Liu, Q. & Guo, D. Emerging coronaviruses: genome structure, replication, and pathogenesis. *J. Med. Virol.* **92**(4), 418–423. https://doi.org/10.1002/jmv.25681 (2020).
9. Lai, C.-C., Shih, T.-P., Ko, W.-C., Tang, H.-J. & Hsueh, P.-R. Severe acute respiratory syndrome coronavirus 2 (SARS-CoV-2) and coronavirus disease-2019 (COVID-19): the epidemic and the challenges. *Int. J. Antimicrob. Agents.* **55**(3), 105924. https://doi.org/10.1016/j.ijantimicag.2020.105924 (2020).
10. Fung, T. S. & Liu, D. X. Human coronavirus: host-pathogen interaction. *Annual Rev. Microbiol.* **73**, 529–557. https://doi.org/10.1146/annurev-micro-020518-115759 (2019).
11. Thiel, V. *et al.* Mechanisms and enzymes involved in SARS coronavirus genome expression. *J. Gen. Virol.* **84**(9), 2305–2315. https://doi.org/10.1099/vir.0.19424-0 (2003).
12. Palese, L.L. The structural landscape of SARS-CoV-2 main protease: hints for inhibitor search. ChemRxiv. https://doi.org/10.26434/chemrxiv.12209744.v1 (2020).
13. Subissi, L. *et al.* One severe acute respiratory syndrome coronavirus protein complex integrates processive RNA polymerase and exonuclease activities. *Proc. Natl. Acad. Sci. USA* **111**(37), E3900-3909. https://doi.org/10.1073/pnas.1323705111 (2014).
14. Kirchdoerfer, R. N. & Ward, A. B. Structure of the SARS-CoV NSP12 polymerase bound to NSP7 and NSP8 co-factors. *Nat. Commun.* **10**(1), 2342. https://doi.org/10.1038/s41467-019-10280-3 (2019).
15. te Velthuis, A. J. W., van den Worm, S. H. E. & Snijder, E. J. The SARS-coronavirus nsp7+nsp8 complex is a unique multimeric RNA polymerase capable of both de novo initiation and primer extension. *Nucleic Acids Res.* **40**(4), 1737–1747. https://doi.org/10.1093/nar/gkr893 (2012).
16. Yang, H., Bartlam, M. & Rao, Z. Drug design targeting the main protease, the Achilles' heel of coronaviruses. *Curr. Pharm. Des.* **12**(35), 4573–4590. https://doi.org/10.2174/138161206779010369 (2006).
17. Pillaiyar, T., Manickam, M., Namasivayam, V., Hayashi, Y. & Jung, S.-H. An overview of severe acute respiratory syndrome-coronavirus (SARS-CoV) 3CL protease inhibitors: peptidomimetics and small molecule chemotherapy. *J. Med. Chem* **59**(14), 6595–6628. https://doi.org/10.1021/acs.jmedchem (2016).
18. Khan, A. *et al.* Phylogenetic analysis and structural perspectives of RNA-dependent RNA-polymerase inhibition from SARs-CoV-2 with natural products. *Interdiscip. Sci.* **12**(3), 335–348. https://doi.org/10.1007/s12539-020-00381-9 (2020).
19. Pokhrel, R., Chapagain, P. & Siltberg-Liberles, J. Potential RNAdependent RNA polymerase inhibitors as prospective therapeutics against SARSCoV-2. *J. Med. Microbiol.* **69**(6), 864–873. https://doi.org/10.1099/jmm.0.001203 (2020).
20. Aouidate, A. *et al.* Identification of a novel dual-target scaffold for 3CLpro and RdRp proteins of SARS-CoV-2 using 3D-similarity search, molecular docking, molecular dynamics and ADMET evaluation. *J. Biomol. Struct. Dyn.* **18**, 1–14. https://doi.org/10.1080/07391102.2020.1779130 (2020).
21. Wu, C. *et al.* Analysis of therapeutic targets for SARS-CoV-2 and discovery of potential drugs by computational methods. *Acta Pharm. Sin. B.* **10**(5), 766–788. https://doi.org/10.1016/j.apsb.2020.02.008 (2020).
22. Surti, M. *et al.* Ilimaquinone (marine sponge metabolite) as a novel inhibitor of SARS-CoV-2 key target proteins in comparison with suggested COVID-19 drugs: designing, docking and molecular dynamics simulation study. *RSC Adv.* **10**, 37707–37720. https://doi.org/10.1039/D0RA06379g (2020).
23. Nikaeen, G., Abbaszadeh, S. & Yousefinejad, S. Application of nanomaterials in treatment, anti-infection and detection of coronaviruses. *Nanomedicine (Lond.)* **15**(15), 1501–1512. https://doi.org/10.2217/nnm-2020-0117 (2020).

24. Palmieri, V. & Papi, M. Can graphene take part in the fight against COVID-19?. *Nano Today* **33**, 100883. https://doi.org/10.1016/j.nantod.2020.100883 (2020).
25. Singla, R., Sharma, C., Shukla, A. K. & Acharya, A. Toxicity concerns of therapeutic nanomaterials. *J. Nanosci. Nanotechnol.* **19**(4), 1889–1907. https://doi.org/10.1166/jnn.2019.16502 (2019).
26. Peng, Z. *et al.* Advances in the application, toxicity and degradation of carbon nanomaterials in environment: a review. *Environ. Int.* **134**, 105298. https://doi.org/10.1016/j.envint.2019.105298 (2020).
27. Innocenzi, P. & Stagi, L. Carbon-based antiviral nanomaterials: graphene, C-dots, and fullerenes: a perspective. *Chem. Sci.* **11**(26), 6606–6622. https://doi.org/10.1039/d0sc02658a (2020).
28. Kraevaya, O. A. *et al.* Direct arylation of $C_{60}Cl_6$ and $C_{70}Cl_8$ with carboxylic acids: a synthetic avenue to water-soluble fullerene derivatives with promising antiviral activity. *Chem. Commun. (Camb)* **56**(8), 1179–1182. https://doi.org/10.1039/C9CC08400B (2020).
29. Dechant, P. P., Wardman, J., Keef, T. & Twarock, R. Viruses and fullerenes—symmetry as a common thread?. *Acta Crystallogr. A Found Adv.* **70**(2), 162–167. https://doi.org/10.1107/S2053273313034220 (2014).
30. Ritter, U. *et al.* Structural features of highly stable reproducible C_{60} fullerene aqueous colloid solution probed by various techniques. *Fullerenes Nanotubes Carbon Nanostruct.* **23**, 530–534. https://doi.org/10.1080/1536383X.2013.870900 (2015).
31. Lim, Y. X., Ng, Y. L., Tam, J. P. & Liu, D. X. Human coronaviruses: a review of virus–host interactions. *Diseases.* **4**(3), 26. https://doi.org/10.3390/diseases4030026 (2016).
32. Prylutskyy, Yu. I. *et al.* On the origin of C_{60} fullerene solubility in aqueous solution. *Langmuir* **30**(14), 3967–3970. https://doi.org/10.1021/la404976k (2014).
33. Grebinyk, A. *et al.* C_{60} fullerene accumulation in human leukemic cells and perspectives of LED-mediated photodynamic therapy. *Free Radic. Biol. Med.* **124**, 319–327. https://doi.org/10.1016/j.freeradbiomed.2018.06.022 (2018).
34. Prylutska, S. V. *et al.* In vitro and in vivo toxicity of pristine C_{60} fullerene aqueous colloid solution. *Fullerenes Nanotubes Carbon Nanostruct.* **27**, 715–728. https://doi.org/10.1080/1536383X.2019.1634055 (2019).
35. Goodarzi, S., Da Ros, T., Conde, J., Sefat, F. & Mozafari, M. Fullerene: biomedical engineers get to revisit an old friend. *Mater. Today.* **20**(8), 460–480. https://doi.org/10.1016/j.mattod.2017.03.017 (2017).
36. Moussa, F. Fullerene and derivatives for biomedical applications. *Nanobiomater* https://doi.org/10.1016/B978-0-08-100716-7.00005-2 (2018).
37. Grebinyk, A. *et al.* C_{60} fullerene as effective nanoplatform of alkaloid berberine delivery into leukemic cells. *Pharmaceutics.* **11**(11), 586. https://doi.org/10.3390/pharmaceutics11110586 (2019).
38. S.V. Eswaran, Water soluble nanocarbon materials: a panacea for all? Curr. Sci. **114**, 1846–1850 (2018). https://doi.org/10.18520/cs/v114/i09/1846-1850
39. Ferreira, C. A., Ni, D., Rosenkrans, Z. T. & Cai, W. Scavenging of reactive oxygen and nitrogen species with nanomaterials. *Nano Res.* **11**(10), 4955–4984. https://doi.org/10.1007/s12274-018-2092-y (2018).
40. Vereshchaka, I. V. *et al.* C_{60} fullerenes diminish the muscle fatigue in rats comparable to N-acetylcysteine or β-alanine. *Front. Physiol.* **9**, 517. https://doi.org/10.3389/fphys.2018.00517 (2018).
41. Lynchak, O. V. *et al.* Comparative analysis of the antineoplastic activity of C_{60} fullerene with 5-fluorouracil and pyrrole derivative in vivo. *Nanoscale Res. Lett.* **12**(1), 8. https://doi.org/10.1186/s11671-016-1775-0 (2017).
42. Zhang, X., Cong, H., Yu, B. & Chen, Q. Recent advances of water-soluble fullerene derivatives in biomedical applications. *Mini-Rev. Org. Chem.* **16**(1), 92–99. https://doi.org/10.2174/1570193X15666180712114405 (2019).
43. https://www.rcsb.org/
44. Yin, W. *et al.* Structural basis for inhibition of the RNA-dependent RNA polymerase from SARS-CoV-2 by remdesivir. *Science* **368**(6498), 1499–1504. https://doi.org/10.1126/science.abc1560 (2020).
45. Chen, P.Y.-T., Li, B., Drennan, C. L. & Elliott, S. J. A reverse TCA cycle 2-oxoacid:ferredoxin oxidoreductase that makes C-C bonds from CO_2. *Joule.* **3**(2), 595–611. https://doi.org/10.1016/j.joule.2018.12.006 (2019).
46. Jurcik, A. *et al.* CAVER Analyst 2.0: analysis and visualization of channels and tunnels in protein structures and molecular dynamics trajectories. *Bioinformatics* **34**(20), 3586–3588. https://doi.org/10.1093/bioinformatics/bty386 (2018).
47. St. John, S. E. *et al.* X-ray structure and inhibition of the feline infectious peritonitis virus 3C-like protease: Structural implications for drug design. *Bioorg. Med. Chem. Lett.* **25**(22), 5072–5077. https://doi.org/10.1016/j.bmcl.2015.10.023 (2015).
48. St. John, S. E., Tomar, S., Stauffer, S. R. & Mesecar, A. D. Targeting zoonotic viruses: Structure-based inhibition of the 3C-like protease from bat coronavirus HKU4-The likely reservoir host to the human coronavirus that causes Middle East Respiratory Syndrome (MERS). *Bioorg. Med. Chem.* **23**(17), 6036–6048. https://doi.org/10.1016/j.bmc.2015.06.039 (2015).
49. Elfiky, A. A. Ribavirin, Remdesivir, Sofosbuvir, Galidesivir, and Tenofovir against SARS-CoV-2 RNA dependent RNA polymerase (RdRp): A molecular docking study. *Life Sci.* **253**, 117592. https://doi.org/10.1016/j.lfs.2020.117592 (2020).
50. UlQamar, M. T., Alqahtani, S. M., Alamri, M. A. & Chen, L.-L. Structural basis of SARS-CoV-2 3CLpro and anti-COVID-19 drug discovery from medicinal plants. *J. Pharmaceut. Anal.* **10**(4), 313–319. https://doi.org/10.1016/j.jpha.2020.03.009 (2020).
51. Warren, G. L. *et al.* A critical assessment of docking programs and scoring functions. *J. Med. Chem.* **49**(20), 5912–5931. https://doi.org/10.1021/jm050362n (2006).
52. McMartin, C. & Bohacek, R. S. QXP: powerful, rapid computer algorithms for structure-based drug design. *J. Comput. Aided Mol. Des.* **11**(4), 333–344. https://doi.org/10.1023/a:1007907728892 (1997).
53. Abraham, M. J. *et al.* GROMACS: high performance molecular simulations through multi-level parallelism from laptops to supercomputers. *SoftwareX.* **1–2**, 19–25. https://doi.org/10.1016/j.softx.2015.06.001 (2015).
54. Huang, J. & MacKerell, A. D. Jr. CHARMM36 all-atom additive protein force field: validation based on comparison to NMR data. *J. Comput. Chem.* **34**(25), 2135–2145. https://doi.org/10.1002/jcc.23354 (2013).
55. Zoete, V., Cuendet, M. A., Grosdidier, A. & Michielin, O. SwissParam: a fast force field generation tool for small organic molecules. *J. Comput. Chem.* **32**(11), 2359–2368. https://doi.org/10.1002/jcc.21816 (2011).
56. https://rashmikumari.github.io/g_mmpbsa/.
57. Kollman, P. A. *et al.* Calculating structures and free energies of complex molecules: combining molecular mechanics and continuum models. *Acc. Chem. Res.* **33**(12), 889–897. https://doi.org/10.1021/ar000033j (2003).
58. Kumari, R., Kumar, R. & Lynn, A. *g_mmpbsa*—a GROMACS tool for high-throughput MM-PBSA calculations. *J. Chem. Inf. Model.* **54**(7), 1951–1962. https://doi.org/10.1021/ci500020m (2014).
59. Wang, J., Wolf, R. M., Caldwell, J. W., Kollman, P. A. & Case, D. A. Development and testing of a general amber force field. *J. Comput. Chem.* **25**(9), 1157–1174. https://doi.org/10.1002/jcc.20035 (2004).
60. Hornak, V. *et al.* Comparison of multiple Amber force fields and development of improved protein backbone parameters. *Proteins* **65**(3), 712–725. https://doi.org/10.1002/prot.21123 (2006).
61. Lindorff-Larsen, K. *et al.* Improved side-chain torsion potentials for the Amber ff99SB protein force field. *Proteins* **78**(8), 1950–1958. https://doi.org/10.1002/prot.22711 (2010).
62. Rocchia, W., Alexov, E. & Honig, B. Extending the applicability of the nonlinear Poisson–Boltzmann equation: Multiple dielectric constants and multivalent ions. *J. Phys. Chem. B* **105**(28), 6507–6514. https://doi.org/10.1021/jp012279r (2001).
63. Weiser, J., Shenkin, P. S. & Still, W. C. Approximate atomic surfaces from linear combinations of pairwise overlaps (LCPO). *J. Comput. Chem.* **20**(2), 217–230 (1999).

64. Gohlke, H., Kiel, C. & Case, D. A. Insights into protein–protein binding by binding free energy calculation and free energy decomposition for the Ras-Raf and Ras–RaIGDS complexes. *J. Mol. Biol.* **330**(4), 891–913. https://doi.org/10.1016/s0022-2836(03)00610-7 (2003).
65. Yan, C. *et al.* Comparative molecular dynamics simulations of histone deacetylase-like protein: binding modes and free energy analysis to hydroxamic acid inhibitors. *Proteins* **73**(1), 134–149. https://doi.org/10.1002/prot.22047 (2008).
66. Muramatsu, T. *et al.* SARS-CoV 3CL protease cleaves its C-terminal autoprocessing site by novel subsite cooperativity. *Proc. Natl. Acad. Sci. USA* **113**(46), 12997–13002. https://doi.org/10.1073/pnas.1601327113 (2016).
67. Li, C. *et al.* Conformational flexibility of a short loop near the active site of the SARS-3CLpro is essential to maintain catalytic activity. *Sci. Rep.* **6**, 20918. https://doi.org/10.1038/srep20918 (2016).
68. Kneller, D. W. *et al.* Structural plasticity of SARS-CoV-2 3CL M proactive site cavity revealed by room temperature X-ray crystallography. *Nat. Commun.* **11**(1), 3202. https://doi.org/10.1038/s41467-020-16954-7 (2020).
69. Yang, H. *et al.* Design of wide-spectrum inhibitors targeting coronavirus main proteases. *PLoS Biol.* **3**(10), e324. https://doi.org/10.1371/journal.pbio.0030324 (2005).
70. Chen, Y. W., Yiu, C.-P.B. & Wong, K.-Y. Prediction of the SARS-CoV-2 (2019-nCoV) 3C-like protease (3CL pro) structure: virtual screening reveals velpatasvir, ledipasvir, and other drug repurposing candidates Version 2. *F1000Res* **9**, 129 (2020).
71. van der Linden, L. *et al.* The RNA template channel of the RNA-dependent RNA polymerase as a target for development of antiviral therapy of multiple genera within a virus family. *PLoS Pathog.* **11**(3), e1004733. https://doi.org/10.1371/journal.ppat.1004733 (2015).
72. Hillen, H. S. *et al.* Structure of replicating SARS-CoV-2 polymerase. *Nature* **584**(7819), 154–156. https://doi.org/10.1038/s41586-020-2368-8 (2020).
73. Gao, Y. *et al.* Structure of the RNA-dependent RNA polymerase from COVID-19 virus. *Science* **368**(6492), 779–782. https://doi.org/10.1126/science.abb7498 (2020).
74. Prylutska, S. *et al.* C_{60} fullerene enhances cisplatin anticancer activity and overcomes tumor cells drug resistance. *Nano Res.* **10**, 652–671. https://doi.org/10.1007/s12274-016-1324-2 (2017).
75. Skivka, L. M. *et al.* C_{60} fullerene and its nanocomplexes with anticancer drugs modulate circulating phagocyte functions and dramatically increase ROS generation in transformed monocytes. *Cancer Nanotechnol.* **9**(1), 8. https://doi.org/10.1186/s12645-017-0034-0 (2018).
76. Kuznietsova, H. *et al.* Water-soluble pristine C_{60} fullerenes inhibit liver fibrotic alteration and prevent liver cirrhosis in rats. *Oxid. Med. Cell. Longev.* **2020**, 8061246. https://doi.org/10.1155/2020/8061246 (2020).
77. Hurmach, Y. *et al.* C_{60} fullerene governs doxorubicin effect on metabolic ptofile of rat microglial cells *in vitro*. *Mol. Pharm.* **17**(9), 3622–3632. https://doi.org/10.1021/acs.molpharmaceut (2020).
78. Choudhury, A. & Mukherjee, S. *In silico* studies on the comparative characterization of the interactions of SARS-CoV-2 spike glycoprotein with ACE-2 receptor homologs and human TLRs. *J. Med. Virol.* **92**(10), 2105–2113. https://doi.org/10.1002/jmv.25987 (2020).

Acknowledgements
This work was supported by the National Research Foundation of Ukraine (grant 2020.01/0044). YIP is grateful to DAAD (Germany) for support.

Author contributions
V.V.H. and M.O.P.: molecular docking. S.V.P. and Y.I.P.: MD simulation. V.V.H. and U.R.: MMPBSA analysis. M.O.P. and P.S.: MMGBSA analysis. S.V.P. and U.R.: analysis of the data and preparing of the manuscript. P.S. and Y.I.P.: coordination of the research work.

Funding
Open Access funding enabled and organized by Projekt DEAL.

Competing interests
The authors declare no competing interests.

Additional information
Correspondence and requests for materials should be addressed to U.R.

Reprints and permissions information is available at www.nature.com/reprints.

Publisher's note Springer Nature remains neutral with regard to jurisdictional claims in published maps and institutional affiliations.

Open Access This article is licensed under a Creative Commons Attribution 4.0 International License, which permits use, sharing, adaptation, distribution and reproduction in any medium or format, as long as you give appropriate credit to the original author(s) and the source, provide a link to the Creative Commons licence, and indicate if changes were made. The images or other third party material in this article are included in the article's Creative Commons licence, unless indicated otherwise in a credit line to the material. If material is not included in the article's Creative Commons licence and your intended use is not permitted by statutory regulation or exceeds the permitted use, you will need to obtain permission directly from the copyright holder. To view a copy of this licence, visit http://creativecommons.org/licenses/by/4.0/.

© The Author(s) 2021